iScience, Volume *24*

Supplemental information

Electric-field-assisted non-volatile magnetic switching in a magnetoelectronic hybrid structure

Yuanjun Yang, Zhenlin Luo, Shutong Wang, Wenyu Huang, Guilin Wang, Cangmin Wang, Yingxue Yao, Hongju Li, Zhili Wang, Jingtian Zhou, Yongqi Dong, Yong Guan, Yangchao Tian, Ce Feng, Yonggang Zhao, Chen Gao, and Gang Xiao

Contents

Data S1: Basic properties of the MgO-based MTJ/(011)-PMN-PT magnetoelectronic hybrid

The MgO-based magnetic tunnel junction/ferroelectric $Pb(Mg_{2/3}Nb_{1/3})_{0.7}Ti_{0.3}O_3$ (MTJ/PMN-PT) magnetoelectronic hybrids were loaded on the probe station after the lithography process and magnetic thermal annealing. As shown in Figure S1(a), the oval-shape MTJs were shown under optical microscopy. The I-V curve measurement with a magnetic bias (H-field) is applied to verify the quality of the MTJs on the ferroelectric PMN-PT substrates. The black and red curves in Figure S1(b) were recorded under large positive (+80 Oe)and negative (–80 Oe) along the major axis of the MTJs, respectively. The two separated curves were indicates two junction resistance states related to the H-fields. Therefore, these two magnetic states should correspond to the antiparallel and parallel magnetization configurations in the MTJs.

To further confirm the above conjecture, the I-V theoretical formula for metal/insulator/metal heterojunctions, which was proposed by Simmons, is applied to fit the two experimental curves (Simmons, 1963). The band alignment of the MTJs is schematically illustrated in Figure S2(a). The current tunneled through the barrier layer (MgO, BL) from the bottom electrode (CoFeB, reference layer, RL) to the top layer (CoFeB, free layer, FL). At a medium-bias voltage, the analytical expression of the current density is (Simmons, 1963):

$$J = \left(\frac{e}{2\pi hs^2}\right)\left\{\left(\varphi_0 - \frac{eV}{2}\right)\exp\left[-\frac{4\pi s}{h}(2m)^{\frac{1}{2}}\left(\varphi_0 - \frac{eV}{2}\right)^{\frac{1}{2}}\right] - \left(\varphi_0 + \frac{eV}{2}\right)\exp\left[-\frac{4\pi s}{h}(2m)^{\frac{1}{2}}\left(\varphi_0 + \frac{eV}{2}\right)^{\frac{1}{2}}\right]\right\} \quad \text{(Formula 1)}$$

where e is the electronic charge, m is the electron mass, h is Planck's constant, s is the thickness of the tunnel junction's insulation layer, V is the voltage that is applied to the tunnel junction, and φ_0 is the barrier height of the MTJ. Considering the good symmetry between the FL and RL and the insulating barrier (MgO), we assumed that $\varphi_1 = \varphi_2 = \varphi_0$ for the fitting process.

In this work, *s* was 2 nm, and φ_0 was approximately 0.58 eV. The fitting results agreed with the experimental results for the antiparallel and parallel states in the medium-bias voltage region, as shown in Figures. S2(b) and S2(c). This result indicates that the MTJs on the ferroelectric PMN-PT substrates had good I-V characteristics and were similar to those that were fabricated on Si wafers (Mazumdar *et al.*, 2008).

Data S2: Repeatability of the angular TMR measurements

We measured the transfer characteristics in many hybrid devices to further check the repeatability of the angular TMR measurements. Figure S3(a) shows a transfer curve (TC) for a typical hybrid device that was measured along the direction of Φ=90°, that is, along the major axis. Figure S3(b) shows a TC that was measured with the H-field fixed along the direction of Φ=50° for another case. The difference in the TMR ratios between the two measurements was only 1%, and the accuracy of the switching field was within ±1 Oe (Safron et al., 2008). These results indicate that our hybrid devices have high quality and good repeatability.

Data S3: Polarization current in the hybrid

The polarization current was recorded to eliminate potentially bad effects on the angular TMR measurements. The electric-field (E-field) scanning began from +6.4 kV/cm, decreased to –6.4 kV/cm, and then returned to its original value in the hybrids. The two peaks around the coercive fields were caused by ferroelectric domain switching, as shown in Figure S(4). The peak polarization current reached ~80 nA under this bipolar E-field cycling. The polarization current was approximately 0.5 nA with unipolar E-field scanning. On the other hand, the current through the tunneling barrier was approximately 0.1 mA in the TMR measurements, nearly six orders of magnitude greater than the polarization current. Therefore, the effects of polarization currents from ferroelectric domain switching could be neglected in the E-field

control of the TMR in this work. Accordingly, the E-field control of magnetic switching must originate from the mechanically strain-mediated magnetoelectric coupling between the FL and PMN-PT ferroelectric substrate. The above results also agree with previous reports for CoFeB/PMN-PT (Zhang *et al.*, 2012), Fe/PMN-PT (Zhang *et al.*, 2017), and Metglas/PMN-PT (Peng *et al.*, 2017) multiferroic heterostructures.

Data S4: Interface effects on strain transfer efficiency

Losses in strain as reported by previous experimental results can be very well explained by the presence of defects or inhomogeneities in the interfaces between the thin films and underneath PMN-PT layers, including intrinsic ferroelastic domain structures after polishing treatment, even cracks of the PMN-PT surface after electric-field cycling, and a possible additional roughness induced during thin-film deposition (Hu *et al.*, 2018; Dorian *et al.*, 2017; Liu *et al.*, 2018). Therefore, the imperfect interface structures, rather than the film thickness, accounts for the strain losses in the transferred strain of the FL in the MTJs/PMN-PT hybrid devices.

Here, we define the strain loss as the strain transfer efficiency (TE) , which is quantified by the relative difference of a strain component ε_y (or ε_x) in the Ta buffer layer (the first layer on substrate surface) and PMN-PT single crystal. The TE is given by (Dorian et al., 2017): $\mathrm{TE}=\frac{\varepsilon_y\ (\mathrm{Simulation})}{\varepsilon_y\ (\mathrm{PMN\text{-}PT})}\times 100\%$, where ε_y (Simulation) is the simulated strain value in the top layer and ε_y (PMN-PT) is the strain induced in the PMN-PT substrate along the *y* axis. For example, a 100% strain transfer means that the ε_{yy} (Simulation) exactly equals the E-field-induced ε_{yy} (PMN-PT).

We adopted the method proposed by Dorian *et al* to qualitatively explore the effect of strain losses due to the imperfect interfaces (Dorian et al., 2017). The truncated pyramid was introduced to mimic the imperfect interfaces between the MTJ and PMN-PT single crystal. To

save computer time, we used one truncated pyramid as shown in Figure S5(a) to estimate the strain transfer efficiency. In addition, the corresponding structure model for the finite element analysis is shown in Figure S5(b).

The transferred strain through the imperfect interfaces can be seen in Figure S6. Figure S6(a), (c) and (e) show the strain (ε_x) distribution in the truncated pyramid under the activated strain state in cases I, II and III as shown in the following Table SI, respectively. Additionally, Figure S6(b), (d) and (f) show the strain (ε_y) distribution in 3-dimensional space is quantified by color-coding. Overall, the strain relaxation is clearly seen from the surface of PMN-PT single crystal to the top of truncated pyramid. In detail, for case I, the strain (ε_x) transfer efficiency (TE) of the surface of the truncated pyramid in the *xoz*-plane is ~97.2% as marked by a white arrow as shown in Figure S6(a), and then reduces to ~89.0% both in case II and III as shown in Figure S6(c) and (e). The strain (ε_x) transfer efficiency (TE) of the edges in case I, II and III is ~86.2% as shown in Figure S6(a), (c) and (e). The strain (ε_y) transfer efficiency (TE) of the surface of the truncated pyramid in the *xoz*-plane and edges are ~89.1% and ~75%, respectively. Therefore, according to the simulations, the strain relaxation and thus non-full strain transfer in the MTJs/PMN-PT is ascribed to the imperfect interfaces. That is why the presence of defects or inhomogeneities on the PMN-PT surface is crucial for the relaxation of strain and hence to explain the losses in the transferred strain into the adjacent MTJ multilayers. Moreover, due to the component multilayer structures of the MTJs, the multi-interfaces between Ta/Ru/Ta/CoFe/IrMn/CoFe/Ru/CoFeB/MgO/CoFeB are also imperfect and thus responsible for the strain relaxation (Dorian *et al.*, 2017).

Although detailed quantitative simulations are not possible due to the interface complexity, the aforementioned simulations still allow a deeper understanding the reasons for losses in the transferred strain in the MTJs/PMN-PT multiferroic heterostructures. Additionally, these

simulations also guide us to further improve the performance of the multiferroic devices through optimizing interface characteristics.

Data S5: Clarifying the conductivity of the barrier and magnetic state on the TMR response

It is well known that the RA product increase exponentially as function of the MgO thickness, which has also been experimentally demonstrated in our previous report (Shen *et al.*, 2005). If a 0.1% change in the MgO thickness will result in an approximate 100% change in the junction resistance (Shen *et al.*, 2006). However, the RA product does not change [~3% in the maximum as marked in Figure S7(a)] so much with increasing *in situ* E-fields as shown in Figure S7(a), definitely indicating that the E-field-induced piezo-strain does not modulate the conductivity of the MgO barrier in our hybrid magnetoelectric devices. Therefore, the one factor of E-field-induced strain on the conductivity of the tunnel barrier can be experimentally exclude in this work.

Naturally, the magnetic state of the FL should be responsible for the E-field control of TMR response. According to the experimental results of the zoom-in Figure S7(b), the RA products of the hybrid in the high-resistance state decrease as increasing E-fields. This result is attributed to the magnetization rotation of the FL by a small angle through the E-field-induced effective magnetic anisotropy with respect to the antiparallel direction (i.e. 180^{o}). For the same reason, the magnetization of the FL rotates by a small angle through the E-field-induced effective magnetic anisotropy with respect to the parallel direction (i.e. 0^{o}), leading to an increase of the RA products as show in Figure S7(c).

Therefore, we can experimentally figure out the effects of the aforementioned two factors: the magnetic states of the free layer and conductivity of the tunnel barrier on the E-field control of TMR using the TC curve measurements.

Data S6: Domain-switching pathway and out-of-plane strain in ferroelectric as revealed by XRD characterizations

The ferroelectric PMN-PT layer was cut along the (011) orientation, which is illustrated as the cyan shaded surface in Figure S8. The in-plane orientations were cut along the [100] and [01-1] orientations. Because of the rhombohedral symmetry of the single crystal (011)-PMN-PT, four equivalent structural ferroelastic domains existed along the body diagonals of the pseudocubic unit cell in the unpoled state, which were labeled as r1 ($r1^+/r1^-$), r2 ($r2^+/r2^-$), r3 ($r3^+/r3^-$), and r4 ($r4^+/r4^-$), as shown in Figure S8 (Nan *et al.*, 2012; Liu *et al.*, 2016).

High-resolution X-ray reciprocal space maps (RSMs) near the (103) reflections of the ferroelectric PMN-PT layer were captured under unipolar E-fields of 0 and 6 kV/cm to qualitatively understand the associated structural ferroelastic domain switching behaviors. The experimental results are shown in Figure S9(a) for 0 kV/cm and Figure S9(b) for 6 kV/cm. Previous structural-domain studies (Liu *et al.*, 2013; Feng *et al.*, 2019; Luo *et al.*, 2013) indicated that cycling the E-field from +6 to 0 kV/cm produced a depolarized state. According to Figure S9(a), the r3 and r4 domains slightly dominated over the $r1^+/r2^+$ domains from the RSM near the (103) reflection of the ferroelectric PMN-PT layer. The dashed ellipses show the r1/r2 and $r3^+/r4^+$ domain positions. When a strong E-field of 6 kV/cm was applied, the RSM of the (103) peak in Figure S9(b) indicated a single peak and a diffused diffraction spot with higher intensity. This result suggests that the r1/r2 structure switched to an $r3^+/r4^+$ structure under a large E-field (Liu *et al.*, 2016).

The ferroelastic domain configuration based on the analysis of the aforementioned experimental data is schematically shown in Figure S9(c) at 0 kV/cm in the depolarized state. The relative intensity is qualitatively shown by the thickness of the arrows. Higher intensity represents more ferroelastic domain variants. Thus, the arrows for the r1/r2 domains are slightly thicker than those for the $r3^+/r4^+$ domains, which is consistent with the experimental result from Figure S9(a). For 6 kV/cm, the $r3^+/r4^+$ domains dominated the intensity of the (103) RSM, as indicated by the thickest arrows in Figure S9(d). Therefore, 71° and 109° of ferroelastic polarization switching from the in-plane direction to the out-of-plane direction occurred after applying a large unipolar E-field, creating large out-of-plane and in-plane tensile strains along the [011] and [01-1] directions and in-plane compressive strain along the [100] direction. The strains are schematically shown by the purple arrows in Figure S9(d). This qualitative result matches the quantitative in-plane strain measurements from Figure S12(b) (see the following section). In addition, this domain switching is reversible by cycling simple unipolar E-fields, which is vital for the reversible E-field control of magnetic switching in magnetoelectronic devices (Liu *et al.*, 2016; Peng *et al.*, 2019).

XRD line scans were performed near the (022) reflection to quantify the out-of-plane strain in response to the aforementioned ferroelastic domain switching. Figure S10(a) shows that the PMN-PT (022) peaks shifted to lower angles as the E-field increased. The corresponding out-of-plane lattice constant and strain (right axis, labeled in blue) are shown in Figure S10(b). The out-of-plane tensile strain reached ~580 ppm under an applied E-field of 6 kV/cm. The shoulder diffraction peak, which reflects the type of ferroelastic domain r1/r2, moved toward the ferroelastic domain r3/r4. Moreover, the shoulder peak intensity decreased as the E-field increased, matching our previous reports (Zhang *et al.*, 2012; Yang *et al.*, 2011) and other studies (Nan *et al.*, 2012; Liu *et al.*, 2016; Liu *et al.*, 2013). Hence, these results further verify the polarization switching pathways in Figures S9(c) and S9(d).

Data S7: Magnetic shape anisotropy of the hybrid

The magnetic shape anisotropy, the E-field-induced magnetoelastic anisotropy (uniaxial anisotropy), and the external magnetic fields jointly determine the angular dependence of the switching fields and TMR ratios in the hybrid. The magnetic shape anisotropy was estimated through TC curves. Without the E-field, the switching fields of the FL are solely determined by the magnetic shape anisotropy of the MTJs (Zhao *et al.*, 2016). The shape anisotropy field can be evaluated from the saturation field of the TC loop in Figure S11 as the H-field was swept along the minor axis of the hybrid device. As shown in the insets of Figure S11, while the magnetization of the FL rotated along the minor axis under the large negative and positive external H-fields, the RA product must have barely changed because of the unchanged orientation of the FL and RL magnetization. The magnetization was saturated by the external H-field, as indicated by the dashed lines in Figure S11. Thus, the saturated H-field H_{Shape} was estimated to be ~100 Oe, and the corresponding shape anisotropy energy was

$$K_{Shape}=\frac{1}{2}H_{Shape}M_s \qquad \text{(Formula 2)}$$

where M_s is the saturated magnetization of the CoFeB for the FL (Zhang *et al.*, 2012). The shape anisotropy energy was calculated to be ~6000 J/m^3. It agrees well with our previous results (Zhao *et al.*, 2016; Chen *et al.*, 2016). This shape anisotropy can compete with E-field-induced magnetoelastic anisotropy, as mentioned in the main text and Table S1 (see the next section). Therefore, the angular dependence of the switching fields and TMR ratios with the assistance of the E-fields was experimentally obtained via TC and CTC measurements by combining the shape anisotropy energy and Zeeman energy from the external H-field.

Data S8: Effective anisotropy field H_{eff} in the FL as induced by E-fields

The strain of the (011)-oriented PMN-PT induced by an E-field was anisotropic, i.e., the compressive strain along the [100] direction and the tensile strain along the [01-1] direction,

because of the opposing ultra-high, in-plane, piezoelectric coefficients. This anisotropic strain transferred to the CoFeB thin film (FL) and introduced biaxial in-plane stresses σ_x and σ_y in the FL. The magnetoelastic energy can be expressed as follows (Liu *et al.*, 2010):

$$F_{me} = -\frac{3}{2}\lambda\sigma_x \sin^2\theta\cos^2\varphi - \frac{3}{2}\lambda\sigma_y \sin^2\theta\sin^2\varphi \qquad \text{(Formula 3)}$$

where θ and φ are the angles defined in Figure S12(a), λ is the in-plane magnetostriction coefficient for the FL, and σ_x and σ_y are the in-plane stress along the [100] and [01-1] directions of the ferroelectric PMN-PT substrate, respectively.

Based on the above magnetoelastic energy, the E-field-induced piezo-strain (or stress) can rotate the magnetization to the position where F_{me} is minimized. F_{me} depends on the square of the sine and cosine functions of the angles θ and φ, so the strain can equal the uniaxial anisotropy and switch the magnetization by 90° at the maximum case. We can reasonably introduce an effective anisotropy field to quantitatively describe the contributions from the E-field-induced piezo-strain in the hybrid as similar to that in conventional multiferroic heterostructures (Dong *et al.*, 2015). Consequently, the minimum value of the following energy expression provides the effective magnetoelastic anisotropy field (H_{eff}) for the FL:

$$F = -\frac{3}{2}\lambda\sigma_x \sin^2\theta\cos^2\varphi - \frac{3}{2}\lambda\sigma_y \sin^2\theta\sin^2\varphi - \mu_0 M_s H_{eff}\cos\varphi \qquad \text{(Formula 4)}$$

For the *+y-axis*, H_{eff} as induced by the in-plane stress is

$$H_{eff,y} = \frac{3\lambda}{M_s}(\sigma_y - \sigma_x) \qquad \text{(Formula 5)}$$

Considering Hooke's law, σ_x and σ_y can be expressed as follows (Liu *et al.*, 2009):

$$\begin{bmatrix}\sigma_x \\ \sigma_y\end{bmatrix} = \frac{Y}{1+\nu}\begin{bmatrix}1 & \nu \\ \nu & 1\end{bmatrix}\begin{bmatrix}\varepsilon_x \\ \varepsilon_y\end{bmatrix} \qquad \text{(Formula 6)}$$

Then,

$$H_{eff,y} = \frac{3Y\lambda}{M_s(1+\nu)}(\varepsilon_y - \varepsilon_x) \qquad \text{(Formula 7)}$$

where Y and ν are Young's modulus and Poisson's ratio for the FL, respectively, and ε_x and ε_y are the in-plane strain along the along the [100] and [01-1] directions of the ferroelectric PMN-PT substrate, respectively. The strain values ε_x and ε_y were measured by using strain gauges, as shown in Figures S12(a) and 12(b).

The E-field-induced H_{eff} can be calculated from the above formula and measured strain values. The corresponding H_{eff} and magnetoelastic anisotropy energy K_u for the micromagnetic simulations are summarized in Table S1.

Data S9: Hard-axis hysteresis loop of unpatterned MTJ multilayers on PMN-PT substrates

Hard-axis hysteresis loops of the unpatterned MTJ multilayers on the PMN-PT substrates were measured with *in-situ* E-fields to further prove the E-field-induced modulation of magnetic anisotropy. As shown in Figure S13(a), the M-H loop was largely slanted at the depolarized state, suggesting that the applied H-field direction should be along the hard axis (*y-axis* of the MTJs). Upon applying an E-field of 6 kV/cm, the M-H loop became a square and easily magnetized, indicating that the magnetic anisotropy rotated in the direction of the *y-axis* through E-field-induced magnetoelastic coupling (Yang *et al.*, 2015; Wang *et al.*, 2013).

Figures S13(b) and S13(c) schematically show that the easy-axis and resultant magnetization (labeled as green arrows) rotated by 90° after applying an E-field. Moreover, the E-field-induced magnetoelastic anisotropy could be restored to its original state if any unipolar E-fields were turned off. This reversible control of magnetic anisotropy and magnetic-switching behaviors with E-fields matches previous results for Ni/(011)-PMN-PT multiferroic heterostructures (Hockel et al., 2012; Hockel et al., 2013).

Data S10: Parameters of micromagnetic simulations for the hybrid

A simple tri-layer structure was adopted to illustrate the physical mechanism of magnetic switching in the FL of the hybrid in the micromagnetic simulations, as shown in Figure S14. This tri-layer structure consisted of three layers, with the FL as the top layer, MgO as the barrier layer, and the RL as the bottom layer. The bottom layer was exchange-biased from the SAF layer, where the dotted arrow shows the direction of the exchange-bias field.

The effective magnetoelastic anisotropy field H_{eff} was set along the crystal axis [01-1] of the PMN-PT ferroelectric layer (or *y-axis* along the hybrid), which was perpendicular to the major axis of the MTJ. The parameters, including Young's modulus, the magnetostriction coefficient, the strain, the uniform exchange constant, the saturation magnetization, the information on the size and shape of the tri-layer structure, and H_{eff}, are all presented in Table S2 for the micromagnetic simulations. Moreover, we optimistically assumed that the piezo-strain could be fully transferred to the FL in the micromagnetic simulations (Biswas *et al.*, 2017).

The size of the device for the micromagnetic simulations was smaller than that of the experimental study to reduce the computational requirement. The length and width in the simulation is same as the experimental case which is tens of micrometers. The magnetization switching insensitively depended on the length of the major and minor axes. Therefore, the exact dimensions did not change the physical mechanism of the E-field-controlled magnetic switching in the hybrid devices at a length scale of tens of microns.

Data S11: E-field-induced magnetization rotation by micromagnetic simulations

Micromagnetic simulations were performed to show the E-field control of magnetization switching in the sandwiched tri-layer of the MTJ based on the above parameters and device architecture. The local moments are shown in small arrows and the macro magnetization is

shown as the large arrow in Figure S15. The FL and RL moment profiles were simulated simultaneously. The upper and lower panels show the simulated moment profiles for the FL and RL, respectively, as shown in Figures S15(a)–S15(d). We first set the initial magnetization along the major axis of the MTJ because of the shape-induced uniaxial anisotropy (Wang et al., 2018), which was along the $+x$ direction or the [100] direction of the PMN-PT substrate. Additionally, we assumed that the device was in a single domain state. The oval-shaped MTJ was within the *x*-*y* plane. The pinning direction of the RL was also along the $+x$ direction. When an E-field of 2 kV/cm was applied, the magnetization rotated towards the induced magnetic easy-axis, which shifted in the $+x$ direction by approximately 30°. When further increasing the E-fields to 4 and 6 kV/cm in Figure S15(c) and S15(d), respectively, the magnetic anisotropy further rotated, and the resultant magnetization of the FL switched to nearly 90°, that is, along the *y-axis*, as shown in Figure S15(d). At a higher E-field of 6 kV/cm, the exchange-biased RL was insensitive to the external H-field and was not modulated significantly by magnetoelastic coupling with the ferroelectric PMN-PT substrate. The magnetization of the RL rotated only approximately 4°, as shown by the yellow arrow in the lower panel of Figure S15(d). This behavior could be ascribed to exchange-bias effects because of the strong RKKY interactions in the SAF structure (Chen et al., 2019). Consequently, the effects of the RL magnetization rotation were neglected, especially in the low-H-field range for the FL magnetization switching, which was also evidenced in a previous work (Li *et al.*, 2014).

In another physical picture, the E-field-induced magnetoelastic anisotropy could be viewed as an effective H-field H_{eff} applied to the FL and RL along the $+y$-*axis*. In addition, the H_{eff} could switch the FL magnetization from the major ($+x$) to the minor ($+y$) axis in the hybrid, as shown in Figures S15(a)–S13(d). This magnetization switching is commonly referred to as strain-induced 90° rotation in multiferroic heterostructures (Zhang *et al.*, 2014; Wang *et al.*, 2018). According to Figure S15, the domain wall generation and propagation are definitely

controlled by E-field-induced H_{eff}, assisting the magnetization rotation of the FL. Consequently, magnetization reversal became easier with the help of the E-field-induced H_{eff}, and 180° switching was subsequently achieved under smaller external H-fields, which were applied along the opposite $-x$ direction. This scheme was experimentally demonstrated in Ta/CoFeB/MgO/CoFeB/(001)-PMN-PT hybrids by Wang *et al.* (Zhao et al., 2016). Here, since the TE was not determined due to the interface complex, for simplicity, we assumed that the strain transferred completely from the PMN-PT to the FL and RL in the micromagnetic simulations (Li *et al.*, 2017; Chavez *et al.*, 2019).

To further understand the magnetic switching process and the jump behavior of the TMR, we performed micromagnetic simulations of the FL in the vicinity of the switching fields. As shown in Figures S16(a1)–S16(a8), for an example, the magnetization 180^o switching from the parallel to antiparallel state is achieved through the vortex domain formation and propagation under a larger negatively H-field bias ($\sim -2.4H_{ES}$) without E-field assistance. When applied the E-field of 6 kV/cm and a relatively smaller H-field ($\sim -H_{ES}$), the Néel domain wall is formed at both ends of the elliptical FL along the x-axis. Then the domain wall propagates to the center of the ellipse and finally completes the magnetization switching, as shown in Figures S16(b1)-S16(b8). This theoretical evidence directly illustrates that the domain wall generation and propagation in the CoFeB thin films under the coactions of the H-fields and E-field-induced strain results in a sharp magnetic switching and subsequently the jump of the TMR in the magnetoelectronic hybrid.

Supplemental figures

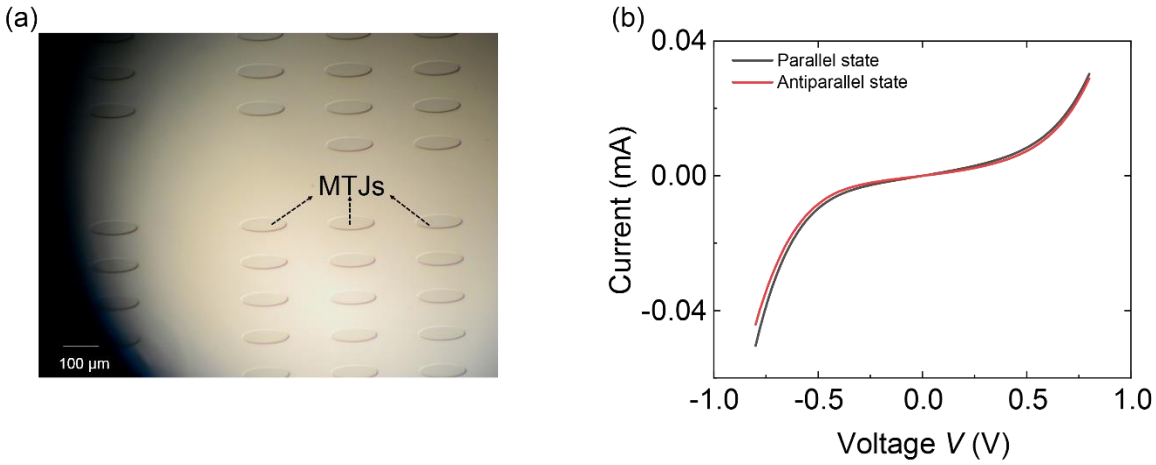

Figure S1. Optical micrograph of the MTJs and typical I-V curves. Related to Figure 1.

(a) Optical micrograph of the MTJs/(011)-PMN-PT magnetoelectronic hybrid devices. (b) I-V curves for the hybrids with parallel and antiparallel magnetization configurations, which are shown in black and red, respectively.

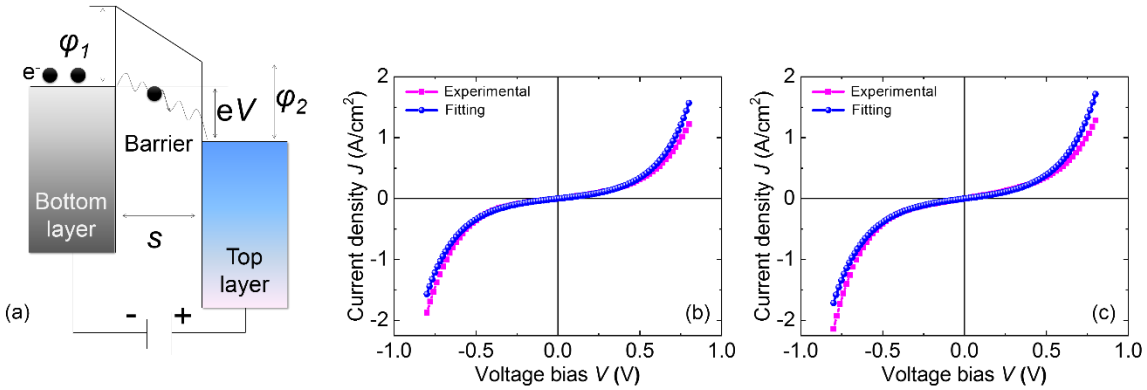

Figure S2. The fitting mode for the MTJ's I-V curves. Related to Figure 2.

(a) Model of the metal/insulator/metal heterojunction to fit the I-V curves of the MTJs in this work. Also shown are the fitting experimental I-V curves for the (b) antiparallel and (c) parallel magnetization configurations.

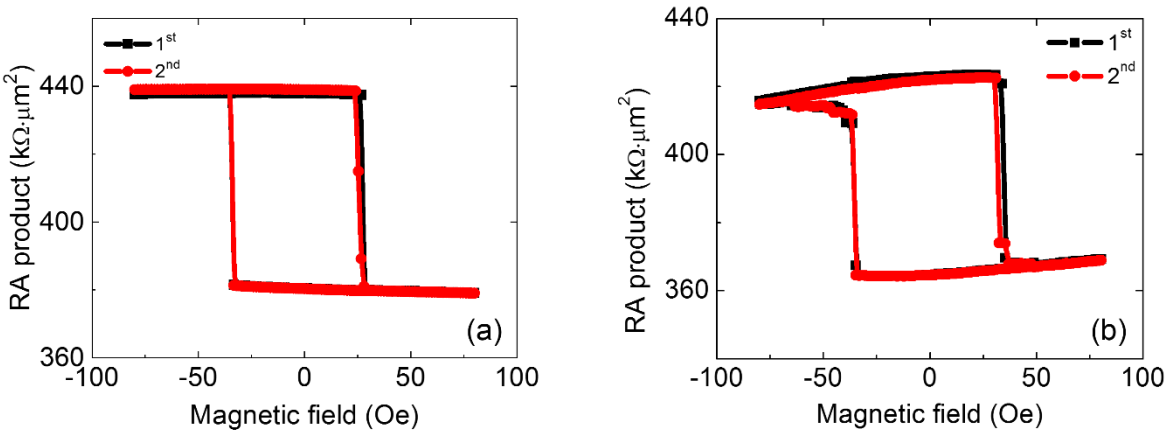

Figure S3. Check measurement repeatability. Related to Figure 2.

Repeated TCs at 0 kV/cm that were measured along the (a) Φ=90° and (b) 50° directions in two hybrid devices.

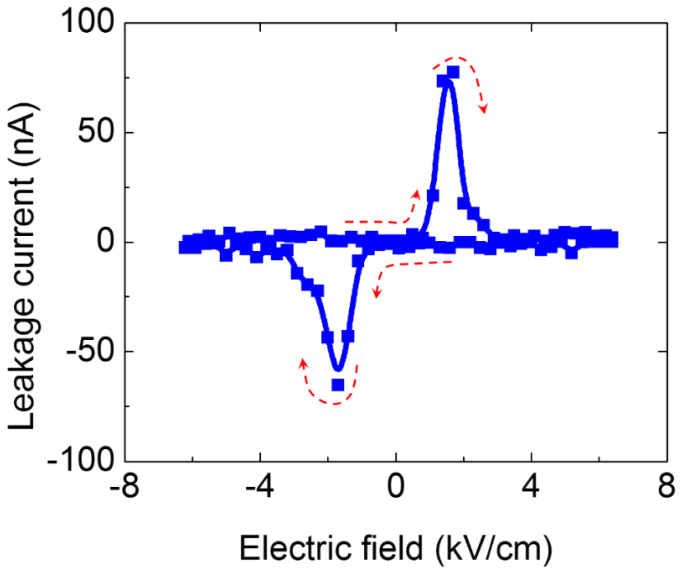

Figure S4. Leakage current during E-field cycling. Related to Figure 2.

Polarization current of the PMN-PT as a function of the applied E-field.

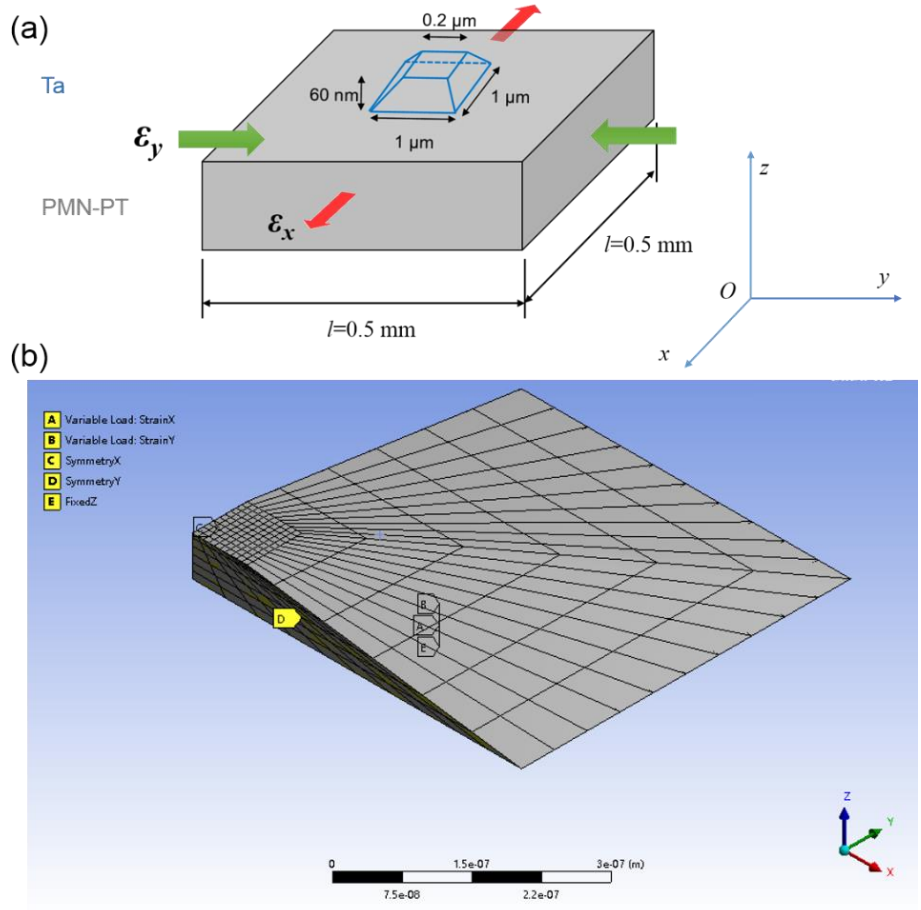

Figure S5. The model for the Finite element method. Related to STAR Methods.

(a) Schematic of a truncated pyramid on the PMN-PT single crystal for finite element simulations. (b) The structural model for the truncated pyramid with simulated meshes.

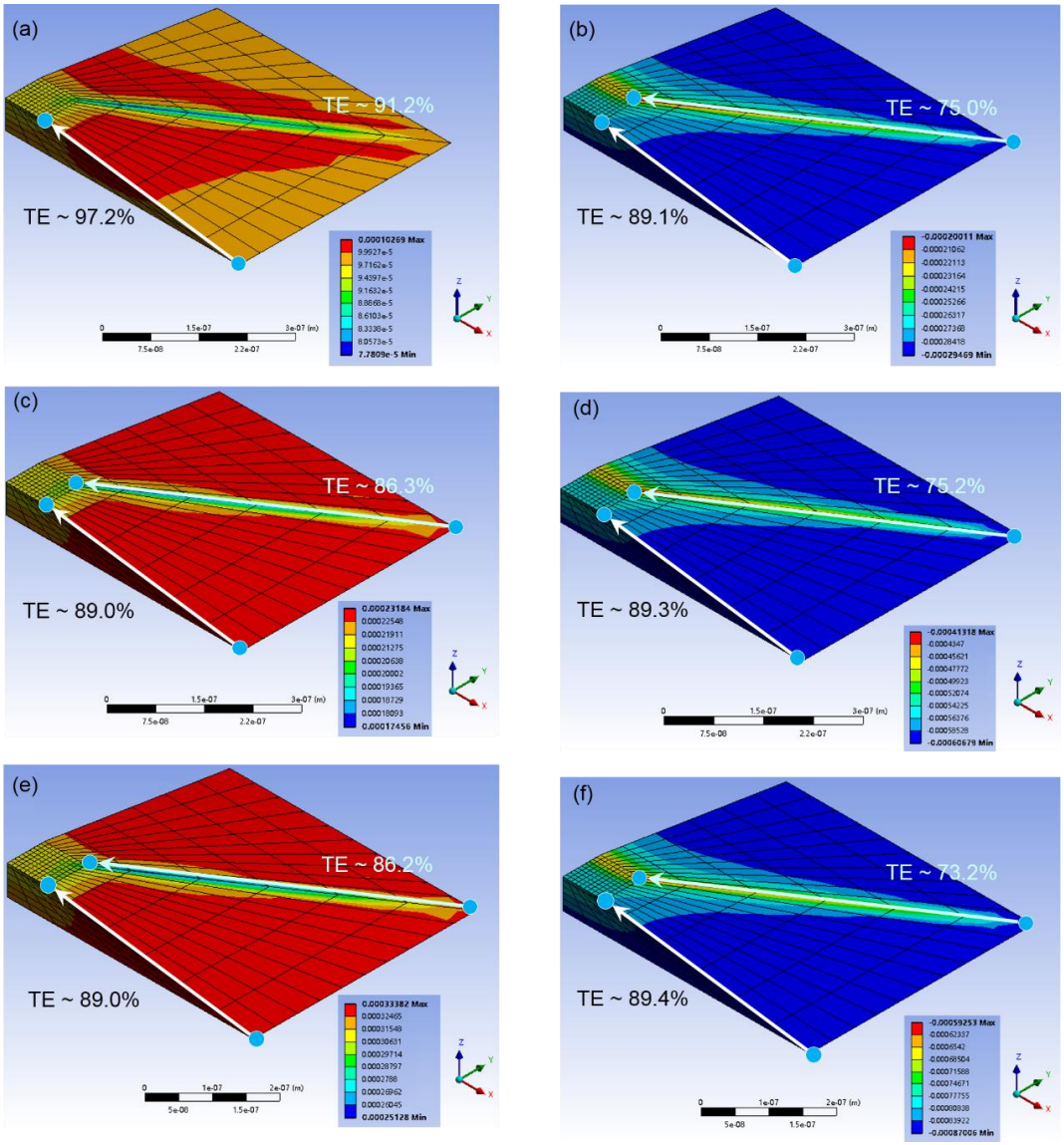

Figure S6. The simulated strain distribution. Related to STAR Methods.

(a), (c) and (e) The strain (ε_x) distribution in the truncated pyramid under the activated strain state in cases I, II and III as shown in Table RI, respectively. (b), (d) and (f) The strain (ε_y) distribution in the truncated pyramid under the activated strain state in cases I, II and III as shown in the following Table S1, respectively.

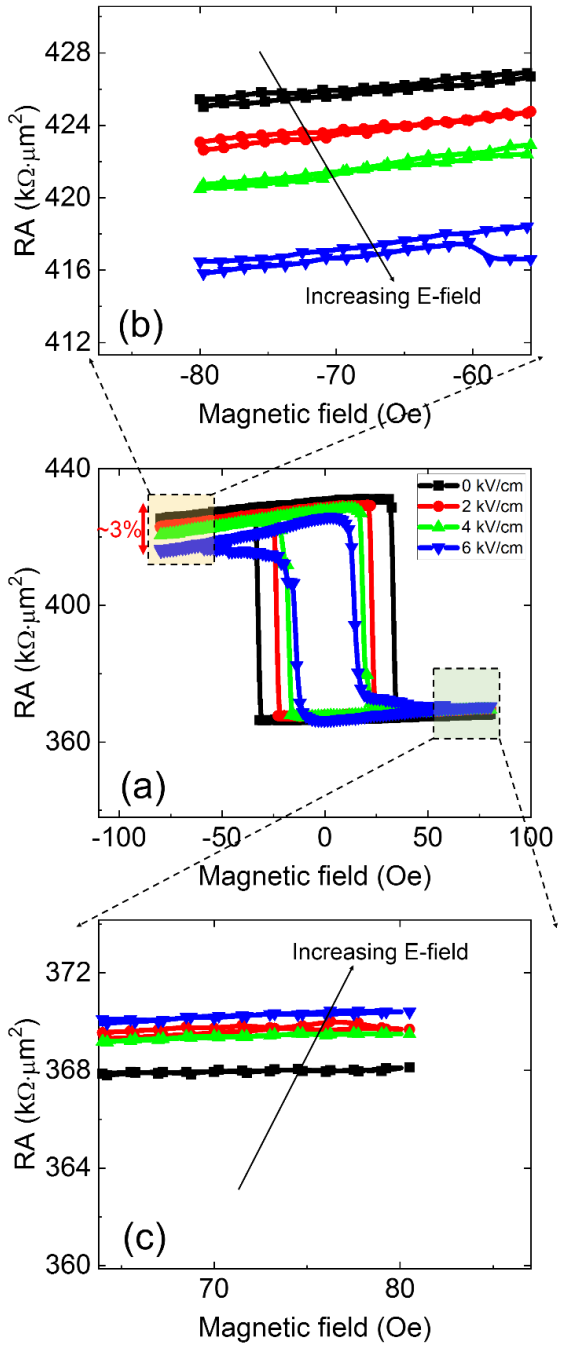

Figure S7. Related to STAR Methods. Related to Figure 5.

(a) RA product is as function of magnetic fields under different E-fields. (b) The enlarged view of (a) as the hybrid device at the high-resistance states. (c) The enlarged view of (a) as the hybrid device at the low-resistance states.

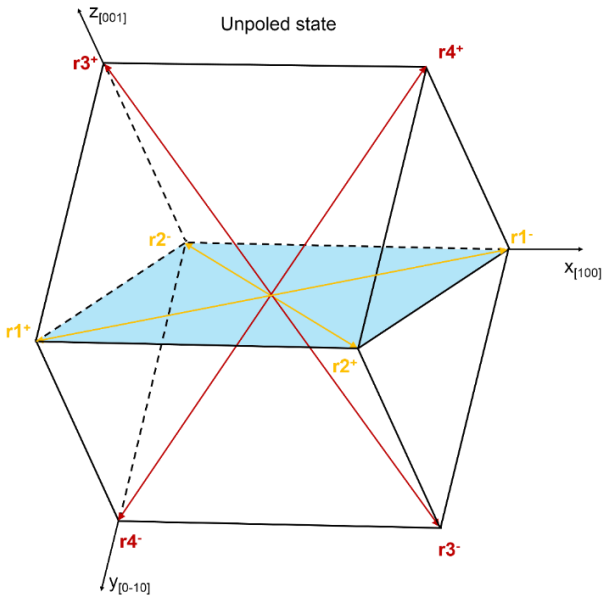

Figure S8. Structural domain configuration. Related to Figure 7.

Schematic of the structural domains in the unpoled ferroelectric (011)-PMN-PT substrate.

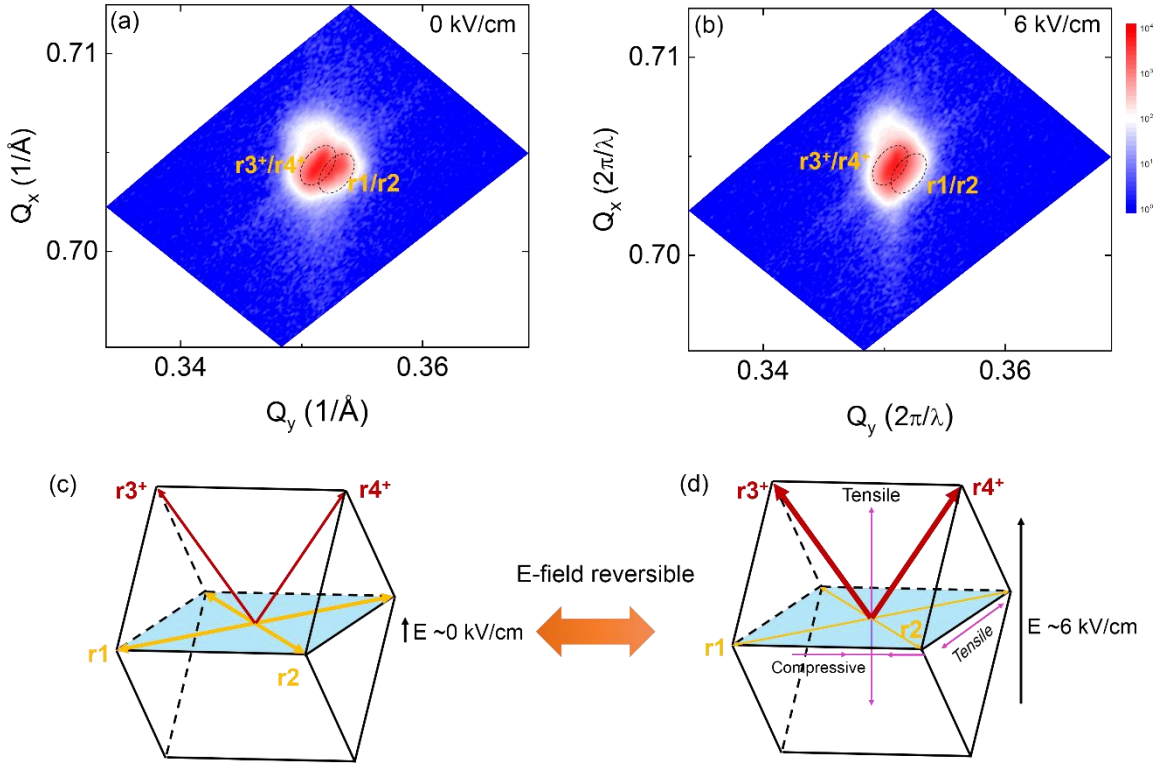

Figure S9. Reciprocal space mapping and domain switching pathway. Related to Figure 7. XRD reciprocal space mappings (RSMs) around the (103) peak of the PMN-PT layer at (a) 0 and (b) 6 kV/cm. Ferroelastic domain configurations for the depolarized state at 0 kV/cm (c) and the polarized state at 6 kV/cm (d). The ferroelastic domain can be reversibly switched by using unipolar E-fields, as schematically shown by the wide orange double arrow.

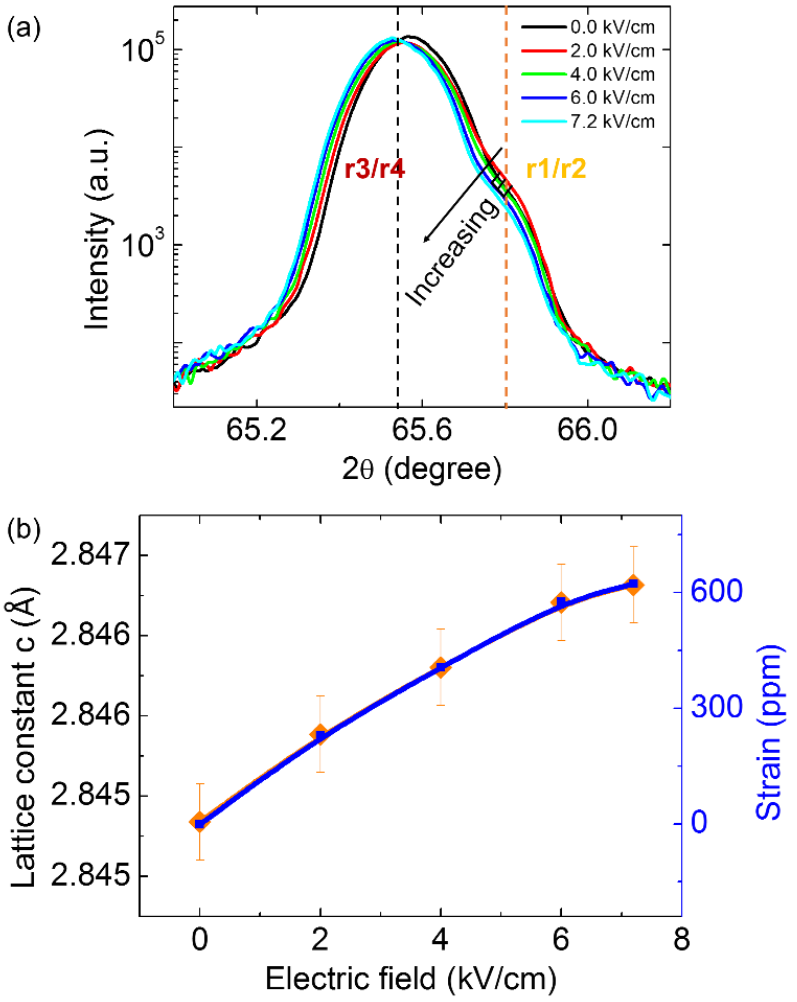

Figure S10. The shift of diffraction peak and corresponding out-of-plane lattice constant and strain. Related to Figure 7.

(a) XRD line scans of the (022) peak for the PMN-PT layer under *in-situ* E-fields. (b) Corresponding out-of-plane lattice constant and strain, which are functions of the E-field.

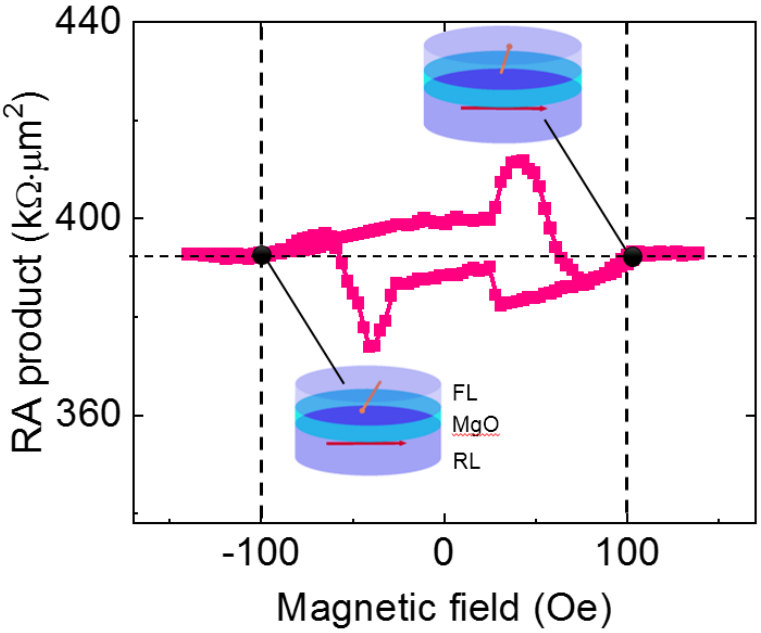

Figure S11. The measurement of saturated magnetic field. Related to Figure 8.

RA product vs. magnetic field along the minor axis of the MTJs in the hybrid devices.

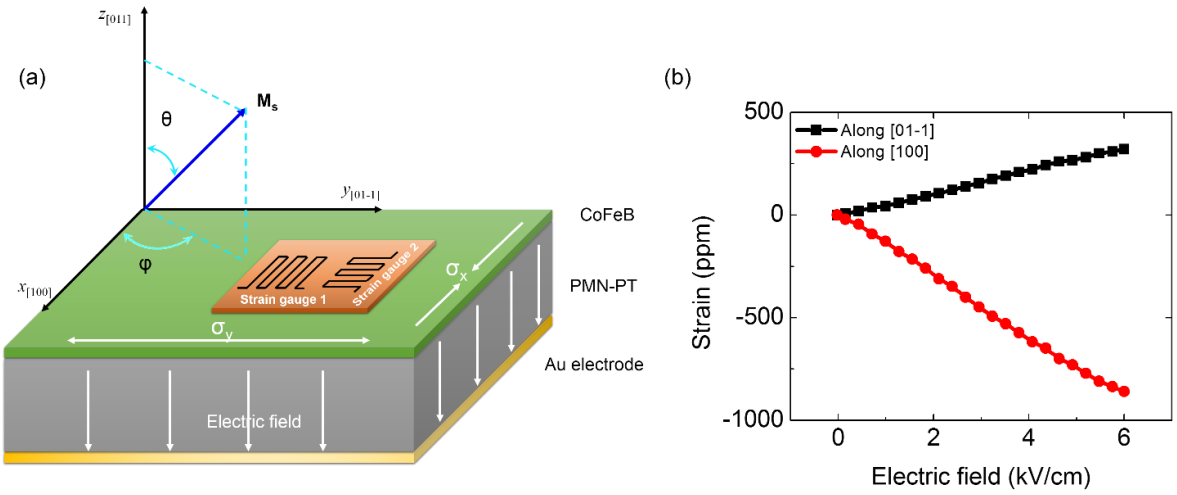

Figure S12. In-plane strain measurement. Related to Figure 8.

(a) Schematic of the magnetization $\mathbf{M_s}$ configuration (angles defined by θ and φ) of the FL under E-field-induced piezo-strain from the ferroelectric PMN-PT substrate. The in-plane piezo-strain along the [100] and [01-1] directions was measured with strain gauges 1 and 2, respectively. (b) Corresponding quantitative strains along the [100] and [01-1] directions, which are functions of the E-fields.

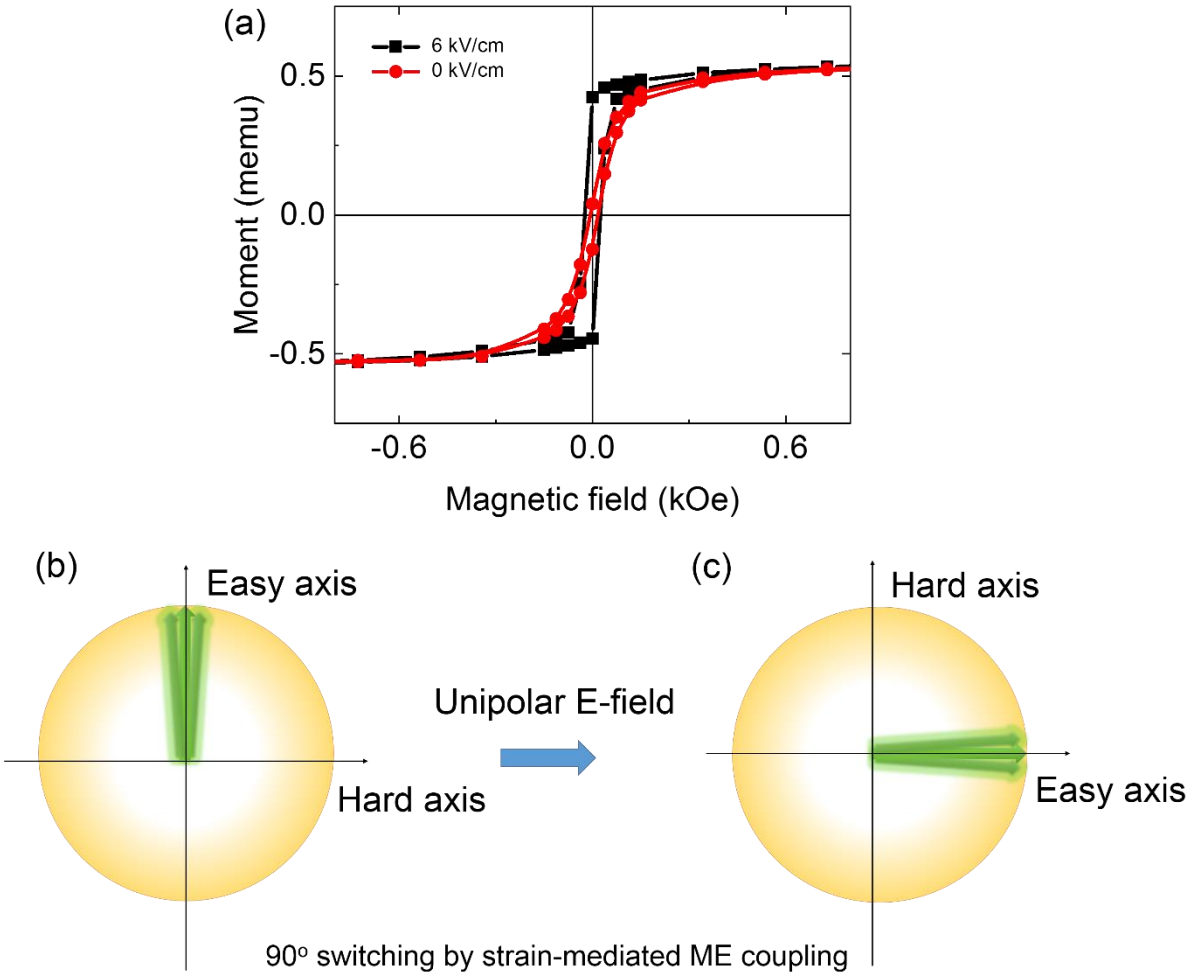

Figure S13. Magnetization rotation under E-field application. Related to Figure 8.

(a) M-H loop measured at the depolarized state with 0 kV/cm and the polarized state with 6 kV/cm. The applied H-field was perpendicular to the direction of the annealing magnetic field, that is, along the hard-axis of the MTJ stacks. (b) and (c) show that the weak magnetic anisotropy, which was induced from magnetic-field annealing, rotated by 90° through magnetoelastic coupling in the unpatterned MTJ/PMN-PT hybrid heterostructures.

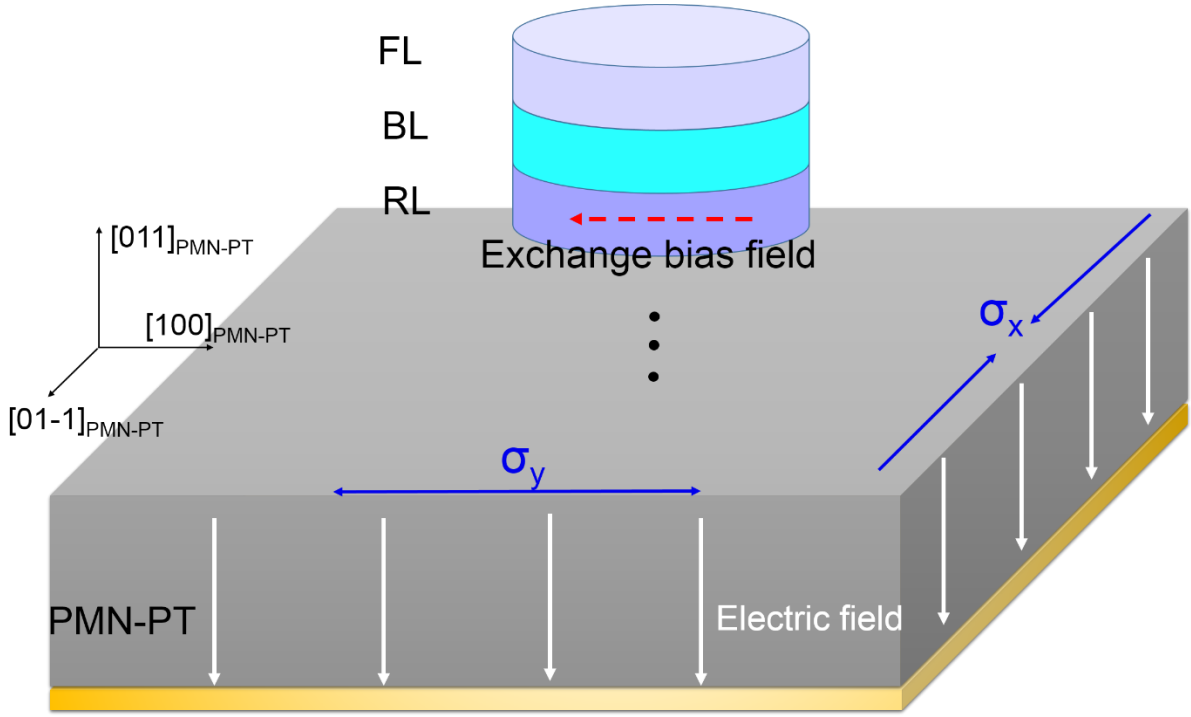

Figure S14. The configuration of simulated hybrid device. Related to Figure 9 and STAR methods.

Schematic of the oval-shaped tri-layer structure on the ferroelectric PMN-PT layer for the micromagnetic simulations.

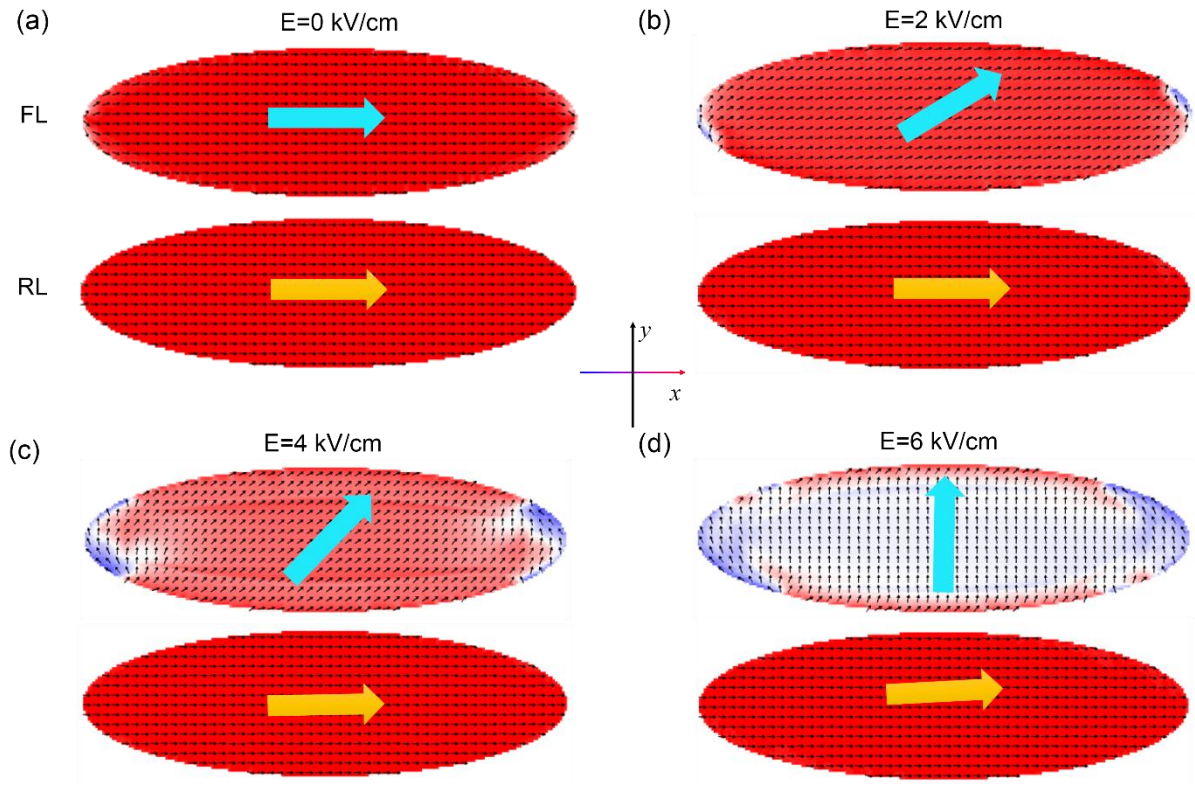

Figure S15. Micromagnetic simulations of the E-field-induced magnetic switching via magnetoelastic coupling between the ferromagnetic FL and RL and the ferroelectric layer in the hybrid. The bias H-field is absent in this case. Related to Figure 9.

The initial parallel configuration for magnetization was after removing the positively saturated H-field along the major axis of MTJ. The micromagnetic simulation profiles of the FL and RL are for the application of E-fields of 0 (a), 2 (b), 4 (c) and 6 kV/cm (d), respectively. The macroscopic magnetization rotated because of the E-fields, as schematically shown with wide cyan and orange arrows in the FL and RL, respectively.

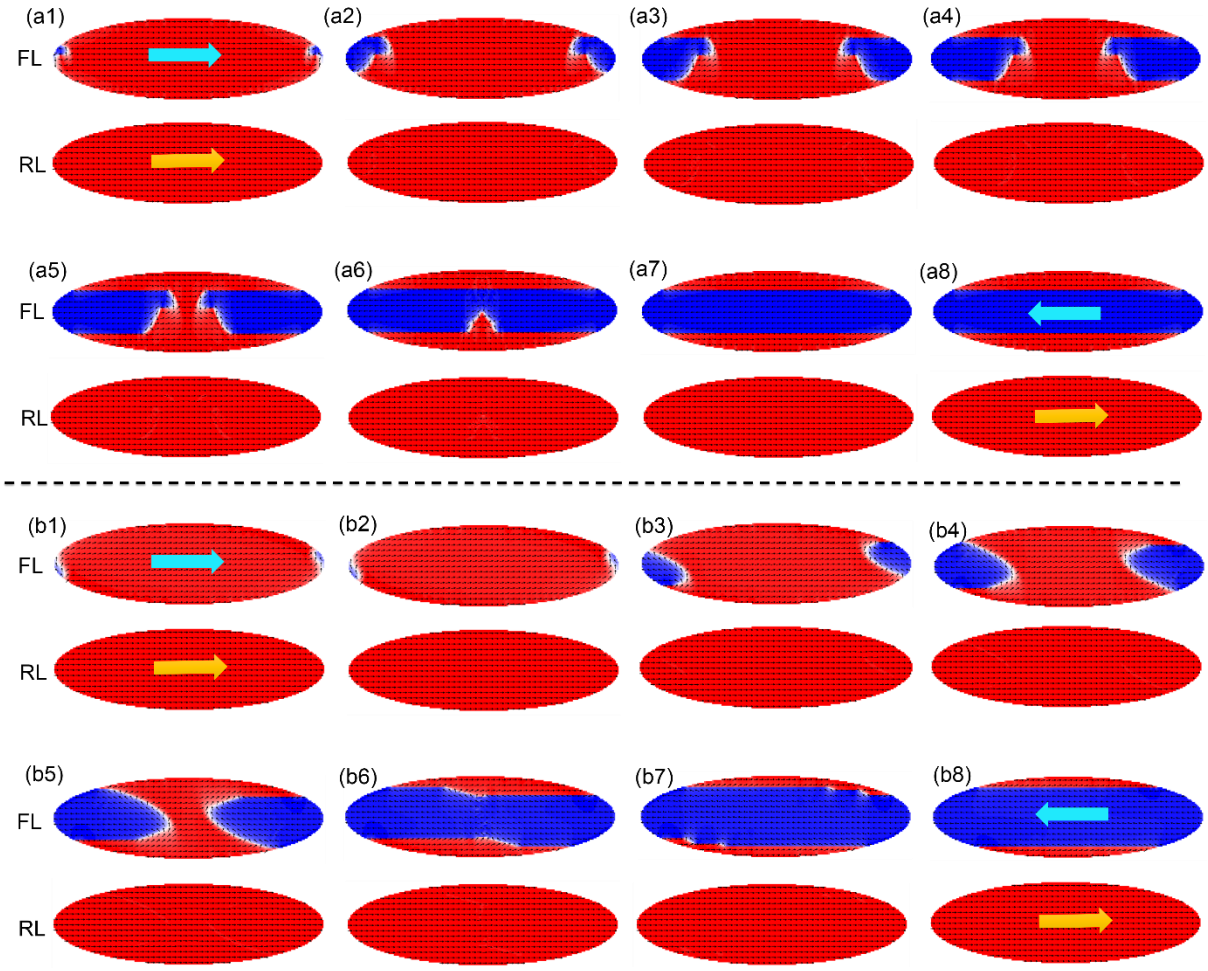

Figure S16. Magnetic switching under coaction of E- and H-fields. Related to Figure 9. (a1)-(a8) The magnetic switching process of the parallel to antiparallel state under a larger H-field (~ $-2.4H_{ES}$) along the $-x$ axis without the assistance of E-field. (b1)-(b8) The magnetic switching process of the parallel to antiparallel state under a relatively smaller H-field (~ $-H_{ES}$) along the $-x$ axis with the assistance of E-field of 6 kV/cm. The initial magnetic sate is in a parallel configuration in both cases as shown in (a1) and (b1). H_{ES} (~11.5 Oe): the switching field of the FL under 6 kV/cm.

Supplemental tables

Table S1. Effective anisotropy field and magnetoelastic anisotropy energy under in-plane anisotropic strain that is induced by some typical E-fields. Related to Figure 8 and STAR Methods.

Strain states of PMN-PT	**Electric field (kV/cm)**	**Strain (ppm) along [100]**	**Strain (ppm) along [01-1]**	**Effective anisotropy field H_{eff} (Oe)**	**Anisotropy energy K_u (J/m^3)**
/	0	0	0	0	0
Case I	2	-291.2	99.5	~50.7	~3000
Case II	4	-599.5	225.8	~107.1	~6400
Case III	6	-859.6	325.2	~153.7	~9200

Table S2. Material parameters for the micromagnetic simulations. Related to Figure 9 and STAR Methods.

Parameters	**Values**	**Note**
Strain (ε)	/	Anisotropic, See Table S1
Young's modulus (Y)	160 GPa	(Hockel et al., 2013)
Magnetostriction (λ)	2×10^{-5}	(Biswas et al., 2017)
Saturation magnetization (M_s)	1.2×10^{6}A/m	Ibid
Exchange constant (A)	2.0×10^{-11} J/m	(Lei, et al., 2013)
Gilbert damping coefficient	0.02	(Zhang et al., 2014)
Shape and size of the free layer	Oval-shape 10 μm × 3 μm × 3 nm	Introducing shape effect of the MTJ in the magnetization switching.
Cell size	50 nm × 50 nm× 3 nm	A relatively larger cell size is adopted to save calculation requirements.
Effective magnetoelastic anisotropy field (H_{eff})	~ 150 Oe	For the case of 6 kV/cm, calculated from the above parameter values by the formula in **Data S8**.

Supplemental references

Lei Zu, Hui Xu, Bing Zhang, Debao Li, Bin Zi. Composite Structures 194, 119–125 (2018).

Jia-Mian Hu, Tiannan Yang and Long-Qing Chen. NPJ Comput. Mater. 4, 62 (2018).

G. Guisbiers, E. Herth, L. Buchaillot, and T. Pardoen. Appl. Phys. Lett. 97, 143115 (2010).

John G. Simmons, J. Appl. Phys. 34, 1793 (1963).

Dipanjan Mazumdar, Weifeng Shen, Xiaoyong Liu, B. D. Schrag, Matthew Carter, and Gang Xiao. J. Appl. Phys. 103, 113911 (2008).

N. S. Safron, B. D. Schrag, X. Y. Liu, W. F. Shen, D. Muzumdar, M. J. Carter, and Gang Xiao. J. Appl. Phys. 103, 033507 (2008).

S. Zhang, Y. G. Zhao, P. S. Li, J. J. Yang, S. Rizwan, J. X. Zhang, J. Seidel, T. L. Qu, Yuanjun Yang, Z. L. Luo, Q. He, T. Zou, Q. P. Chen, J.W. Wang, L. F. Yang, Y. Sun, Y. Z. Wu, X. Xiao, X. F. Jin, J. Huang, C. Gao, X. F. Han, and R. Ramesh. Phys. Rev. Lett. 108, 137203 (2012).

Sen Zhang, Qianping Chen, Yan Liu, Aitian Chen, Lifeng Yang, Peisen Li, Zhou Shi Ming, Yi Yu, Wen Sun, Xiaozhong Zhang, Yuelei Zhao, Young Sun, and Yonggang Zhao. ACS Appl. Mater. Interfaces 9, 20637 (2017).

Bin Peng, Chenxi Zhang, Yuan Yan, and Ming Liu. Phys. Rev. Appl. 7, 044015 (2017).

Dorian Ziss, Javier Martín-Sánchez, Thomas Lettner, Alma Halilovic, Giovanna Trevisi, Rinaldo Trotta, Armando Rastelli, and Julian Stangl. J. Appl. Phys. 121, 135303 (2017).

Z. Q. Li, J. H. Liu, M. D. Biegalski, J.-M. Hu, S. L. Shang, Y. Ji, J. M. Wang, S. L. Hsu, A. T. Wong, M. J. Cordill, B. Gludovatz, C. Marker, H. Yan, Z. X. Feng, L. You, M. W. Lin, T. Z. Ward, Z. K. Liu, C. B. Jiang, L. Q. Chen, R. O. Ritchie, H. M. Christen & R. Ramesh. Nature Communications 9, 41 (2018).

Weifeng Shen, X. Y. Liu, D. Mazumdar and Gang Xiao. Appl. Phys. Lett. 86, 253901 (2005).

Weifeng Shen, D. Mazumdar, X. Zou, X. Liu and Gang Xiao. Effect of film roughness in MgO-based Magnetic Tunnel Junctions. Appl. Phys. Lett. 88, 182508 (2006).

T. X. Nan, Z. Y. Zhou, J. Lou, M. Liu, X. Yang, Y. Gao, S. Rand, and N. X. Sun. Appl. Phys. Lett. 100, 132409 (2012).

Ming Liu, Tianxiang Nan, Jia-Mian Hu, Shi-Shun Zhao, Ziyao Zhou, Chen-Ying Wang, Zhuang-De Jiang, Wei Ren, Zuo-Guang Ye, Long-Qing Chen & Nian X Sun. NPG Asia Materials 8, e316 (2016).

Ming Liu, Brandon M. Howe, Lawrence Grazulis, Krishnamurthy Mahalingam, Tianxiang Nan, Nian X. Sun, and Gail J. Brown. Adv. Mater. 25, 4886 (2013).

Ce Feng, Yan Liu, Haoliang Huang, Zhaozhao Zhu, Yuanjun Yang, You Ba, Shuying Yan, Jianwang Cai, Yalin Lu, Jinxing Zhang, Sen Zhang, and Yonggang Zhao. ACS Appl. Mater. Interfaces 11, 25569 (2019).

Zhenlin Luo, Zuhuang Chen, Yuanjun Yang, Heng-Jui Liu, Chuanwei Huang, Haoliang Huang, Haibo Wang, Meng-Meng Yang, Chuansheng Hu, Guoqiang Pan, Wen Wen, Xiaolong Li, Qing He, Thirumany Sritharan, Ying-Hao Chu, Lang Chen, and Chen Gao. Phys. Rev. B 88, 064103 (2013).

Yuanjun Yang, Z. L. Luo, Haoliang Huang, Yachun Gao, J. Bao, X. G. Li, Sen Zhang, Y. G. Zhao, Xiangcun Chen, Guoqiang Pan, and C. Gao. Applied Physics Letters 98, 153509 (2011).

Zhengyang Zhao, Mahdi Jamali, Noel D'Souza, Delin Zhang, Supriyo Bandyopadhyay, Jayasimha Atulasimha, and Jian-Ping Wang. Appl. Phys. Lett. 109, 092403 (2016).

Aitian Chen, Yonggang Zhao, Peisen Li, Xu Zhang, Renci Peng, Haoliang Huang, Lvkuan Zou, Xiaoli Zheng, Sen Zhang, Peixian Miao, Yalin Lu, Jianwang Cai, and Ce-Wen Nan. Adv. Mater. 28, 363 (2016).

Ming Liu, Ogheneyunume Obi, Zhuhua Cai, Jing Lou, Guomin Yang, Katherine S. Ziemer, and Nian X. Sun. J. Appl. Phys. 107, 073916 (2010).

Shuai Dong, Jun-Ming Liu, Sang-Wook Cheong & Zhifeng Ren. Advances in Physics 64, 519 (2015).

Ming Liu, Ogheneyunume Obi, Jing Lou, Yajie Chen, Zhuhua Cai, Stephen Stoute, Mary Espanol, Magnum Lew, Xiaodan Situ, Kate S. Ziemer, Vince G. Harris, Nian X. Sun. Adv. Funct. Mater. 19, 1826 (2009).

Yuanjun Yang, Yongqi Dong, Meng Meng Yang, Hao He, Bin Hong, Z. L. Luo, Haoliang Huang, Haibo Wang, Mengjiao Wang, Xiaodi Zhu, J. Bao, X. G. Liu, J. Y. Zhao, X. G. Li and C. Gao. EPL 109, 17008 (2015).

J. W. Wang, Y. G. Zhao, C. Fan, X. F. Sun, S. Rizwan, S. Zhang, P. S. Li, Z. Lin, Yuanjun Yang, W. S. Yan, Z. L. Luo, L. K. Zou, H. L. Liu, Q. P. Chen, X. Zhang, M. H. Zhu, H. Y. Zhang, J. W. Cai, X. F. Han, Z. H. Cheng, C. Gao, D. Xie, and T. L. Ren. Appl. Phys. Lett. 102, 102906 (2013).

Joshua L. Hockel, Alexandre Bur, Tao Wu, Kyle P. Wetzlar, and Gregory P. Carman. Appl. Phys. Lett. 100, 022401 (2012).

Hockel, J. L., Pollard, S. D., Wetzlar, K. P., Wu, T., Zhu, Y., & Carman, G. P. Appl. Phys. Lett. 102, 242901 (2013).

Ayan Kumar Biswas, Hasnain Ahmad, Jayasimha Atulasimha, and Supriyo Bandyopadhyay. Nano Lett. 17, 3478 (2017).

Lei, N.; Devolder, T.; Agnus, G.; Aubert, P.; Daniel, L.; Kim, J.; Zhao, W.; Trypiniotis, T.; Cowburn, R. P.; Chappert, C.; Ravelosona, D.; Lecoeur, P. Nat. Commun. 4, 1378 (2013).

Sen Zhang, Yonggang Zhao, Xia Xiao, Yizheng Wu, Syed Rizwan, Lifeng Yang, Peisen Li, Jiawei Wang, Meihong Zhu, Huiyun Zhang, Xiaofeng Jin & Xiufeng Han. Sci. Rep. 4, 3727 (2014).

Qianchang Wang, John Domann, Guoqiang Yu, Anthony Barra, Kang L. Wang, and Gregory P. Carman. Phys. Rev. Appl. 10, 034052 (2018).

A. Chen, Y. Zhao, Y. Wen, L. Pan, P. Li, X.-X. Zhang. Sci. Adv. 5, eaay5141 (2019).

Peisen Li, Aitian Chen, Dalai Li, Yonggang Zhao, Sen Zhang, Lifeng Yang, Yan Liu, Meihong Zhu, Huiyun Zhang, and Xiufeng Han. Adv. Mater. 26, 4320 (2014).

Peisen Li, Yonggang Zhao, Sen Zhang, Aitian Chen, Dalai Li, Jing Ma, Yan Liu, D. T. Pierce, J. Unguris, Hongguang Piao, Huiyun Zhang, Meihong Zhu, Xiaozhong Zhang, Xiufeng Han, Mengchun Pan, and Cewen Nan. ACS Appl. Mater. Interfaces 9, 2642 (2017).

Andres C. Chavez, Joseph D. Schneider, Anthony Barra, Sidhant Tiwari, Robert N. Candler, and Gregory P. Carman. Phys. Rev. Appl. 12, 044071 (2019).